ACCSCIENCE PUBLISHING

Journal of Seismic Exploration

ARTICLE

Pore structure characterization for carbonate rocks using the adaptively weighted learning scheme

Bonan Li[1]*, Feng Zhu[2], and Xuebing Zhang[3]

[1]College of Transportation Engineering, Nanjing Tech University, Nanjing, Jiangsu, China

[2]East China Branch, SINOPEC Petroleum Engineering Geophysics Co., LTD., Nanjing, Jiangsu, China

[3]School of Earthquake Sciences and Technology, Institute of Disaster Prevention, Sanhe, Hebei, China

Abstract

The hydrocarbon reserves and permeability of carbonate reservoirs are controlled by the microscopic heterogeneity of pore geometries and constituent components, collectively referred to as pore structure. Nevertheless, the geophysical characterization of pore structures is generally constrained by the intrinsic difficulty of direct observation and the theoretical complexity of the associated rock-physics models. Accordingly, as an extension and integration of conventional measurement-driven and model-driven workflows, this study proposes to construct a pore structure classifier based on an adaptive machine learning framework. Firstly, to improve the data quality of the original core sample set, we developed a tailored data-model hybrid training set, which is labeled based on microscopic dominant pore geometries and characterized by macroscopic elastic property features. In this hybrid set, we extended the range and density of rock-physics measurements by incorporating abundant virtual carbonate samples generated through the differential effective medium theory guided by a random procedure. Secondly, to mitigate potential biases in the classifier's training procedure, an adaptive dual trade-off weighting system is devised to address the issues of imbalance (cored versus modeled samples) and skewness (majority versus minority samples) in the raw sample distribution. Thirdly, the proposed weighted data-model-driven framework outperforms pure data-driven methods, pure model-driven methods, and unweighted methods in both classification accuracy and model robustness for the pore structure characterization task. Our approach proves effective in characterizing the vertical heterogeneity of pore structure, enabling accurate reserve estimation and providing critical insights for inferring geological history from logging data.

Keywords: Carbonate rock; Pore structure; Rock-physics model; Weighted learning machine

***Corresponding author:**
Bonan Li
(libn@njtech.edu.cn)

Citation: Li B, Zhu F, Zhang X. Pore structure characterization for carbonate rocks using the adaptively weighted learning scheme. *J Seismic Explor.* doi: 10.36922/JSE026250110

Received: June 19, 2026

Revised: August 26, 2026

Accepted: September 3, 2026

Published online: September 23, 2026

Copyright: © 2026 Author(s). This is an Open-Access article distributed under the terms of the Creative Commons Attribution License, permitting distribution, and reproduction in any medium, provided the original work is properly cited.

Publisher's Note: AccScience Publishing remains neutral with regard to jurisdictional claims in published maps and institutional affiliations.

1. Introduction

As ideal hydrocarbon reservoirs, carbonate rocks are usually characterized by highly diversified pore structures, which are formed by different geological processes acting

on brittle matrices over long geological periods.[1,2] Existing imaging studies have confirmed that moldic and vuggy dissolution processes yield approximately spherical pore geometries in carbonate rocks, whereas tectonic fracturing and natural cracking generate flat pore morphologies.[3-5] This microscopic pore heterogeneity not only affects the storage capacity and migration efficiency of hydrocarbons, but also preserves the key spatio-temporal evolutionary information of carbonate reservoirs.[6,7]

In terms of pore structure characterization methods, scholars consider that indirect approaches utilizing macroscopic data have greater application prospects than costly direct observation methods based on micro-computed tomography (CT) and thin sections.[8,9] Specifically, if a natural rock is regarded as a composite material containing internally multiscale pore systems, its pore composition can be indirectly inverted based on the rock-physics response differences of macroscopic data acquired from multiple scales, including core analysis, well logging, and seismic exploration.[10,11] However, the performance of existing indirect pore characterization methods, including both model-based and data-based paradigms, is consistently constrained by the quality of acquired geophysical data. Model-based methods, typified by the dichotomy method and the flexibility factor method, characterize pore structure by solving an inverse problem of a predefined rock-physics model.[12-14] In contrast, data-based methods tend to learn rock-physics response patterns from labeled known samples that have ideal data structure and scale, and then extend the learned patterns to unlabeled, unknown data.[15-17] However, it is widely recognized that in practical applications, both model complexity and data quality are largely uncontrollable factors. For instance, the majority of existing rock-physics models for unconventional reservoirs are characterized by high complexity and strong nonlinearity, while their observed data acquired from laboratory experiments and field surveys differ significantly in structural characteristics and spatial scale.[3,4] To bridge this gap, although the recently proposed data-model integrated scheme has exhibited favorable performance, it still fails to resolve the learning bias induced by the inherent label imbalance in rock-physics measurement data.[18]

To address the aforementioned challenges in carbonate rock pore structure characterization—specifically, the ambiguous multi-solution dilemma of pure model-driven methods and the data quality limitation of pure data-driven methods—this paper proposes an adaptive framework for building a data-model integrated classifier, which is embedded with a dual trade-off mechanism along with a tailored training set construction and optimization workflow. The first systematically implemented dual trade-off scheme adaptively supervises the machine learning process by incorporating both the actual observation results of core samples and the theoretical rock-physics constraints of carbonate rocks, enabling the constructed classifier to mitigate two inherent biases in laboratory measurements that restrict the performance of traditional methods: label imbalance induced by the diversity of pore structures, and limited core sample availability caused by the brittleness of carbonate rocks. Results from laboratory experiments and logging tests demonstrate that, compared with conventional unweighted single-source machine learning classifiers, the proposed scheme achieves substantial improvement in both prediction accuracy and robustness.

2. Methods

This section outlines the target categories of carbonate pore structures and the feature space they are mapped to, and highlights different approaches for indirect pore structure characterization.

2.1. Rock-physics theory of carbonate rocks

2.1.1. Modeling of multi-structured pore systems

Pore structure refers to the geometry, size, distribution, and connectivity of microscopic voids in rock.[4] Existing imaging studies have demonstrated that, due to their inherent brittleness and solubility, the pore systems of carbonate rocks, which formed through long-term regional geological evolution, predominantly develop characteristic fractal patterns rather than irregular pore structures.[19,20] From the perspective of geological origin, as systematically summarized by Lucia,[18] carbonate reservoirs develop extremely complex multi-type pore assemblages formed by the superposition of sedimentation, compaction, and multi-stage diagenesis. Such pore assemblages cover interparticle pores, intraparticle pores, moldic pores, separate vugs, touching vugs, and microfracture voids. Although the geological origin of pore structures in carbonate rocks is complex and heterogeneous, the macroscopic elastic response of such rocks—the core rock-physics relationships—depends almost entirely on the dominant aspect ratio of pore spaces, rather than the minor variations in fabric structure and connectivity among pores sharing identical geometric morphology.[4,12,14] Therefore, based on the principle of rock-physics grouping equivalence, this study adopted a simplified framework that categorizes the diverse natural pore subtypes into three representative endmembers in accordance with their characteristic roundness, through which geologically distinct but elastically equivalent pore populations are merged into aggregations.[18]

- (#1) "Flat pores" are planar voids with aspect ratios smaller than 0.05 that form in the presence of directed geological stresses, such as fractures and microcracks.
- (#2) "Elliptic pores" are ellipsoidal voids with aspect ratios of 0.10 to 0.30 that occur between individual particles, grains, or crystals, such as interparticle and intraparticle pores.
- (#3) "Spherical pores" are large, spherical voids with aspect ratios greater than 0.50 that originate from the selective dissolving of minerals, such as vugs, cavities, moldic pores, and leached grains.

Notably, this simplification strikes a balance between geological authenticity and the computational efficiency of the fast differential effective medium (DEM) rock-physics modeling workflow. As a result, it cannot distinguish between fine subclasses within a single aspect-ratio regime (e.g., separating isolated vugs from touching vugs in permeability or capillary-pressure-focused reservoir evaluation tasks).

Under controlled laboratory conditions, pore structures can be reliably extracted and accurately classified from micro-CT scan images (Figure 1). From this perspective, the total rock porosity φ can be expressed as the sum of the fractional porosities corresponding to each pore structure component (**Equation 1**):

$$\begin{aligned} &\varphi_i = v_i \varphi \\ &\sum_{i=1}^{I} v_i = 1 \end{aligned} \tag{1}$$

where φ is the total porosity, I is the number of pore structures, φ_i denotes the fractional porosity of the i-th pore structure component, and v_i is its corresponding fraction of pore volume.[20,21]

2.1.2. Modeling of elastic responses

Elastic properties are observable geophysical parameters that reflect the elastic wave propagation characteristics of rocks (e.g., elastic modulus, wave velocity, density, Poisson's ratio) through macroscopic measurements (e.g., ultrasonic testing, well logging, seismology).[4,8] Compared to direct imaging observations, indirectly inferring pore structure at the macroscopic scale is more efficient and practical. In this process, rock-physics models play a critical role in linking microscopic and macroscopic rock properties. Among these models, DEM theory has been proven to perform well for multi-structured porous media such as carbonate rock.[21] A standard DEM, as **Equation 2** indicates, predicts elastic modulus by repeatedly substituting tiny inclusions into the host material:[22]

$$\begin{aligned} (1-y)\frac{dK^*(y)}{dy} &= \left[K_i - K^*(y)\right]P^{*i} \\ (1-y)\frac{dG^*(y)}{dy} &= \left[G_i - G^*(y)\right]Q^{*i} \end{aligned} \tag{2}$$

where K and G are the bulk and shear moduli. As specified in *Berryman*, the polarization scalars P and G are functions of pore geometry, and the inclusion volume y equals porosity.[23]

Existing studies indicate that the numerical solution of this coupled ordinary differential equation suffers from high computational time consumption and path dependence.[22,23] Aiming at addressing this limitation, this work adopted a decoupled approximation scheme derived from the original model, namely the fast DEM method, to implement large-scale modeling of research samples. This approach (**Equation 3**) maintains the advantages of the original DEM and yields efficiency enhancements of up to a thousand times by removing its iterative calculations:[24]

$$\begin{cases} K_{\mathrm{d}}^*(\varphi) = K_{\mathrm{m}}(1-\varphi)^{\sum_{i=1}^{I} v_i (P_0^i + P_1^i)} e^{\varphi \sum_{i=1}^{I} v_i P_1^i} \\ G_{\mathrm{d}}^*(\varphi) = G_{\mathrm{m}}(1-\varphi)^{\sum_{i=1}^{I} v_i (Q_0^i + Q_1^i)} e^{\varphi \sum_{i=1}^{I} v_i Q_1^i} \end{cases} \tag{3}$$

Here, K_{d} and G_{d} are the drained elastic moduli. Subscript "m" denotes mineral properties. Subscripts "1" and "2" denote the decomposition orders of P and Q.[24] Subsequently, the density, compressional wave (P-wave) velocity (V_{p}) and shear wave (S-wave) velocity (V_{s}) of the saturated rock samples can be obtained via prediction (Appendix A).

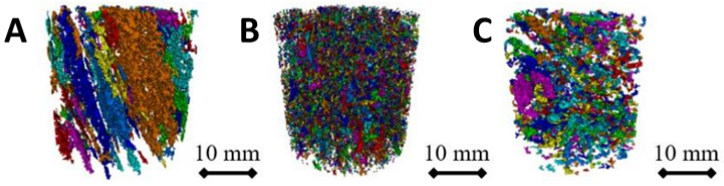


Figure 1. Typical three-dimensional images obtained via micro-computed tomography scanning, including samples dominated by pore structures. (A) Flat pores. (B) Elliptical pores. (C) Spherical pores.

Based on this theoretical framework, this study constructed numerical simulation cases to quantitatively reveal the mechanisms by which pore shape, pore volume, and pore content influenced the macroscopic elastic properties of rocks. To eliminate the interference of lithological heterogeneity on the numerical simulation results, this study simplified the rock matrix to pure dolomite, thereby ensuring that pore parameters are the only variable in the subsequent numerical simulation cases. Accordingly, the mineral bulk modulus (K) and shear modulus (G) can be calculated using mixing laws, such as the Voigt–Reuss–Hill averaging. Thus, the two parameters were treated as constants of 96 GPa and 45 GPa, respectively, in this simulation, as reported by Mavko *et al.*[4] With this simplification, Figure 2 presents an example of rock-physics modeling results obtained for a dry carbonate rock skeleton. This study's results indicate that rock stiffness exhibits a distinct dependence on both total pore volume and pore morphology. The analysis further demonstrated that cracked rocks contained a higher proportion of compressible pore space than porous rocks with equivalent total porosity, and consequently exhibited lower elastic wave velocity. To further investigate the influence mechanism of pore composition on elastic properties, Figure 3 presents the modeling results for a drained dolomite sample with fixed porosity (10%) and pore aspect ratios, but varied volume proportions of different pore components. Represented by characteristic vectors, aspect ratios for flat, elliptical, and spherical pores, $\alpha = [\alpha_1, \alpha_2, \alpha_3]$, were set to [0.01, 0.20, 0.80], in line with widely accepted conventions in the published works.[1,5,13,21] We found that pure vuggy rocks had the highest wave velocity, and pure cracked rocks had the lowest. When pore space contained more than one type of pore component, the dominant pore structure (position) can affect the sample velocity (color) by more than 50%. This means that using elastic properties to characterize the dominant pore structure is reasonable.

Thereby, in the construction of the feature space, we leveraged the fundamental elastic property that both compressional wave (P-wave) velocity (V_p) and shear wave (S-wave) velocity (V_s), as well as rock density (ρ), exhibited high sensitivity to pore volume and pore structure, and could be readily obtained from multi-source observation data. Accordingly, a three-dimensional feature space defined as $x = [V_p, V_s, \rho]$ was established in this study.[5]

2.1.3. Review of pore structure characterization methods

Pore structure characterization is commonly used to detect

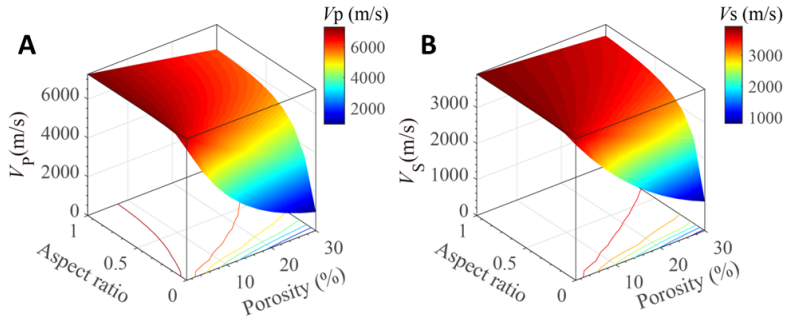


Figure 2. Predicted wave velocities of rocks with a single pore constituent but varying porosity and aspect ratio. (A) P-wave velocity. (B) S-wave velocity. The axes correspond to pore aspect ratio, porosity, and wave velocity, respectively.

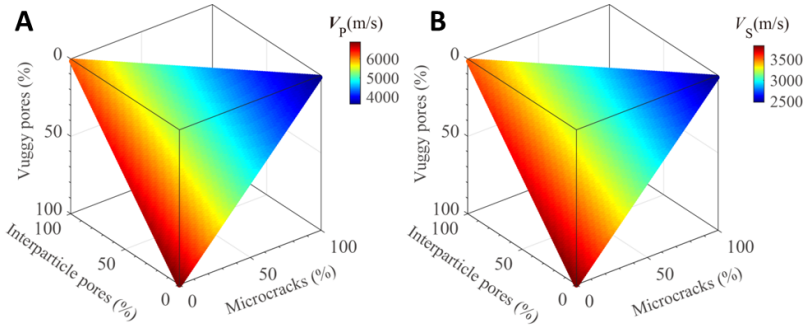


Figure 3. Predicted wave velocities of rocks with ternary pore constituents, fixed porosity, and fixed aspect ratio. (A) P-wave velocity. (B) S-wave velocity. Colors indicate velocity magnitude. The axes correspond to the volume fractions of microcracks, interparticle pores, and vuggy pores.

the dominant pore component in rock.[25] Figure 4 shows that our target is to infer an unknown physical property vector m of a rock sample from its observed feature $\boldsymbol{x}$.[26] Here, we have $\boldsymbol{m} = [\varphi, v, \alpha]$, and $\boldsymbol{x} = [V_p, V_s, \rho]$. To achieve this goal, there are three possible routes, which are data-based, model-based, and data-model-based.

Data-based methods map samples to predefined structure labels. The relationship between feature x and label y is first built on well-known samples, and then generalized to unknown labels $\boldsymbol{y}^*$. Nevertheless, the performance efficiency of such methods is highly sensitive to the quality of training data. Typically, to maximize the classification accuracy on observed training samples, classifiers tend to shift the decision boundary toward classes with smaller sample sizes. Common data defects can be summarized into two types: (i) the data imbalance problem caused by technical constraints, including borehole deployment, coring interval selection, and core preparation difficulties; (ii) the data skewness problem arising from inconsistent scale comparability among core analysis data, well logging data, and seismic data.[27]

Model-based methods solve for unknown m^* through inverse rock-physics models $g^{-1}()$, i.e., $\boldsymbol{m}^* = g^{-1}(\boldsymbol{x}^*)$. However, if $g()$ is a nonlinear or irreversible model, such as the DEM (**Equations 2** and **3**), the solving processes of $g^{-1}()$ are usually time-consuming and non-stationary. As shown in Figure 3, each m (position) can be mapped to a unique x (color), whereas a given observed x^* might correspond to more than one pore system m^*.

This study proposes a data-model-based classifier that adopts a dual trade-off weighting strategy to adaptively supervise the machine learning process, using both actual core observation results and theoretical rock-physics constraints. It not only retains the statistical characteristics of the original core dataset but also exploits the computational convenience of theoretical models, while completely obviating the complexity of inversion processing.

2.2. Weighted learning scheme for pore structures

This section elaborates on the approaches to improving the data quality of the training set, constructing the adaptively weighted classifier, and applying the constructed classifier to pore structure characterization.

2.2.1. Weighted classifier with dual trade-off

A weighted variant of the support vector machine (w-SVM) was adopted to handle complex data distribution scenarios. The proposed w-SVM can rebalance the training procedure by assigning misclassification weights to individual samples within the cost function (**Equation 4**):[28]

$$\begin{aligned} &\min_{\boldsymbol{\omega},b} \frac{1}{2}\boldsymbol{\omega}^{\mathrm{T}}\boldsymbol{\omega} + C\sum_{i=1}^{N} w_i\xi_i \\ &s.t.\, \boldsymbol{y}_i\left(\boldsymbol{\omega}^{\mathrm{T}}\phi(\boldsymbol{x}_i)+b\right) \geq 1-\xi_i, \xi_i \geq 0 \end{aligned} \tag{4}$$

where C is the penalty, ξ is the learning error, and w is the weight. Thus, the weights of all samples are represented by the vector $\boldsymbol{w} = \left\{w^{(n)}\right\}_{n=1}^{N}$. As shown in **Equation 5**, the kernel $\phi()$ is determined as the radial basis function (RBF) in this paper to enhance data separability:[29]

$$\kappa(x_i, x_j) = e^{-\gamma\left\|x_i - x_j\right\|^2} \tag{5}$$

where γ is the hyperparameter of the RBF kernel.

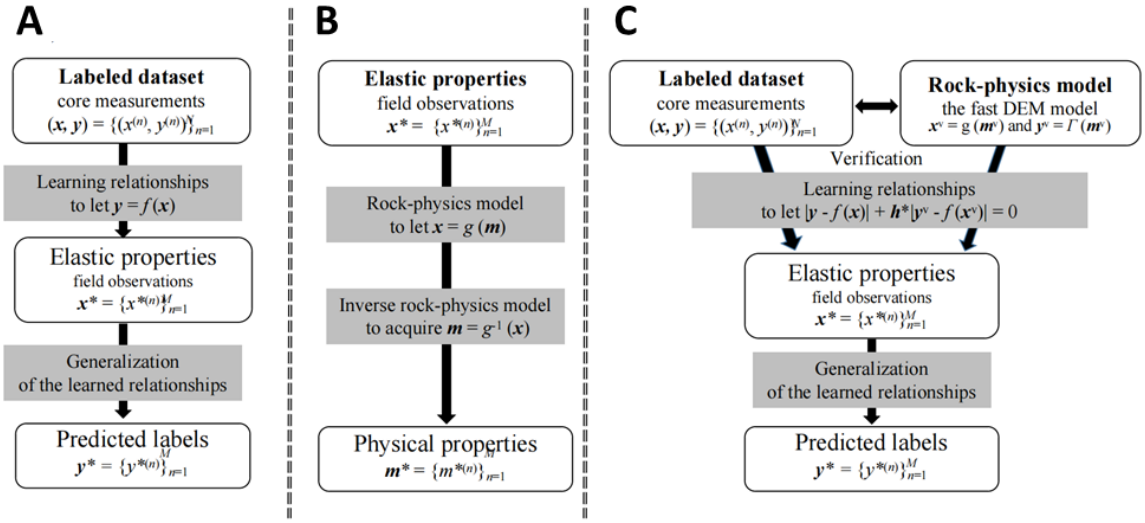


Figure 4. Major routes for indirect pore structure characterization. (A) Pure data-based method. (B) Model-based method. (C) Data-model-based method.

In this paper, we propose a dual trade-off system consisting of a class weight $\boldsymbol{w}_1$ and a source weight $\boldsymbol{w}_2$, such that $\boldsymbol{w} = \boldsymbol{w}_1 \times \boldsymbol{w}_2$:

(i) $\boldsymbol{w}_1$ compensates for the minority class in the raw sample set (or weakens the majority class).
(ii) $\boldsymbol{w}_2$ decides the relative priority of the modeled and measured samples in the cost function.

Specifically, the multiplicative weighting structure of w satisfies both mathematical interpretability and physical independence. From the perspective of mathematical logic, given the orthogonality between the two weighting objectives, the sample weight is constructed as the multiplicative product $\boldsymbol{w}_1 \times \boldsymbol{w}_2$ rather than an additive combination. The class weight $\boldsymbol{w}_1$ corrects intra-source label imbalance, while the source weight $\boldsymbol{w}_2$ adjusts inter-source distribution skewness, with no functional overlap between the two terms. This product structure treats both bias corrections as independent scaling factors for sample loss penalties, facilitating simultaneous, decoupled optimization of class balance and data-source balance. In contrast, an additive weight formulation would linearly interfere with the penalty scaling of these terms, thereby undermining the classification accuracy of minority pore samples.

We first analyze the parameter $\boldsymbol{w}_1$. As presented in **Equation 6**, when equal weights are assigned to all samples within the same pore structure class, the weight of each individual sample is proportional to the scarcity of its corresponding class label in the training set,[28] that is:

$$w_1^{(n)} = \frac{N_{\text{train}}}{\sum_{i=1}^{N_{\text{train}}} 1\left(y^{(i)} = y^{(n)}\right)} \tag{6}$$

where $1(\cdot)$ equals 1 if the condition inside the parentheses is satisfied, and 0 otherwise, and N_{train} is the total number of samples in the training set.

To facilitate evaluation of the defect type and degree within a dataset, the imbalance ratio (IR) and skewness ratio (SR) are introduced as evaluation indicators, as shown in **Equation 7**:

$$IR = \frac{\max_{k\in\{1,2,\ldots,I\}} N_k}{\min_{k\in\{1,2,\ldots,I\}} N_k}, \quad SR = \frac{N_{\text{test}}}{N_{\text{train}}} \tag{7}$$

where N_{test} is the total number of samples in the test set, and N_k is the number of samples belonging to the k-th pore structure label. From this perspective, a robust classifier requires a minimal test-to-training ratio (low SR) and relatively equal numbers of training samples across classes (low IR).

This paper examined and compared the unweighted and weighted classifiers on the standard dichotomous dataset "banana," following the experimental setup of previous research by Zong *et al.*[30]As shown in Figure 5, the unweighted support vector machine (SVM) classifier achieved effective training when using the ideal subset of the "banana" dataset (Figure 5A**,** 5B). In contrast, when the same classifier was trained on the defective dataset extracted at an IR of 20, the number of misclassified samples increased significantly (Figure 6). The decision boundary of the SVM, marked by the red curve, shifted toward the minority class region in the feature space, which ultimately led to an 18% increase in the misclassification rate (Figure 6D). Although slight classification distortion remained, the introduced trade-off weight w_1 (where point size reflects the weighting value) adjusted the decision boundary back to the correct intermediate position, achieving a classification accuracy of 99% (Figure 7).

2.2.2. Enhancing rock-physics characteristics

Improving the data quality, which is usually limited by unpredictable coring conditions, of the training set is another way to boost classifier performance. Accordingly, to augment the information capacity of the original core dataset, the proposed scheme leverages the computational efficiency of theoretical rock-physics models. Its implementation consists of four sequential procedures: virtual sample generation, sample annotation, property prediction, and dataset mixing.

(i) Based on core statistical characteristics, the virtual sample $S^{v(0)}$ with physical property vector $\boldsymbol{m}^{v(0)}=[\boldsymbol{\varphi}^{(0)}, \boldsymbol{f}^{(0)}, \boldsymbol{v}^{(0)}, \boldsymbol{\alpha}^{(0)}]$ is randomly generated through the virtual sample generation (VSG) workflow. The complete implementation of the VSG procedure is elaborated in detail in Appendix B. In the notation above, the superscript "v" indicates that the corresponding parameter belongs to the virtual sample, and φ, $\boldsymbol{f}$, $\boldsymbol{v}$, and $\boldsymbol{\alpha}$ denote the total porosity, mineralogy vector, pore composition vector, and aspect ratio vector of such virtual sample, respectively.
(ii) The label $y^{v(0)}$ of $S^{v(0)}$ corresponds to the position of the maximum element in the vector $\boldsymbol{v}^{v(0)}$.
(iii) The elastic responses of $S^{v(0)}$, $\boldsymbol{x}^{v(0)} = [V_p^{v(0)}, V_s^{v(0)}, \rho^{v(0)}]$ are predicted by substituting $\boldsymbol{m}^{v(0)}$ into the fast DEM model, $g(\boldsymbol{m}^{v(0)})$.
(iv) After repeating steps (i) to (iii), a hybrid set $\boldsymbol{S}$ is rebuilt by mixing $\boldsymbol{S}^c$ and $\boldsymbol{S}^v$ with an expected proportion and scale. This hybrid $\boldsymbol{S}$ can provide a lower IR and SR than the original $\boldsymbol{S}^c$; the pseudo-code for the generation of virtual samples and the construction of the hybrid sample set is provided in Figure A1.

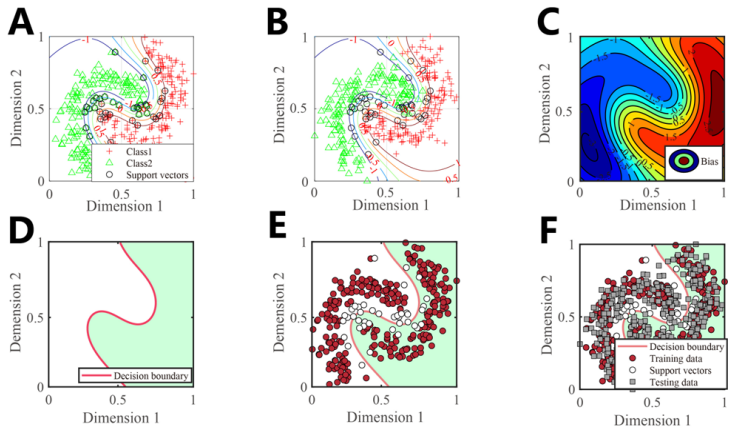


Figure 5. Classification results of the unweighted support vector machine (SVM) classifier on a balanced dataset. (A) Training set and corresponding support vectors. (B) Test set. (C) Bias contour. (D) Decision boundary of the SVM classifier. (E) Support vectors, decision boundary, and training set. (F) Support vectors, decision boundary, training set, and test set. Different point shapes denote distinct classes.

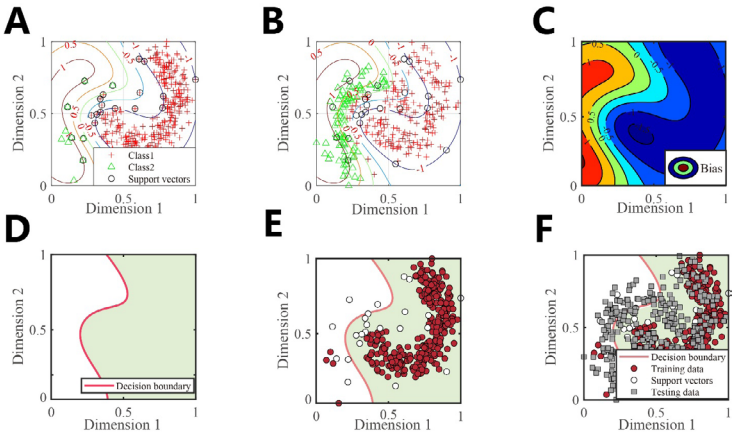


Figure 6. Classification results of the unweighted support vector machine (SVM) classifier on an imbalanced dataset. (A) Training set and corresponding support vectors. (B) Test set. (C) Bias contour. (D) Decision boundary of the SVM classifier. (E) Support vectors, decision boundary, and training set. (F) Support vectors, decision boundary, training set, and test set. Different point shapes represent distinct classes.

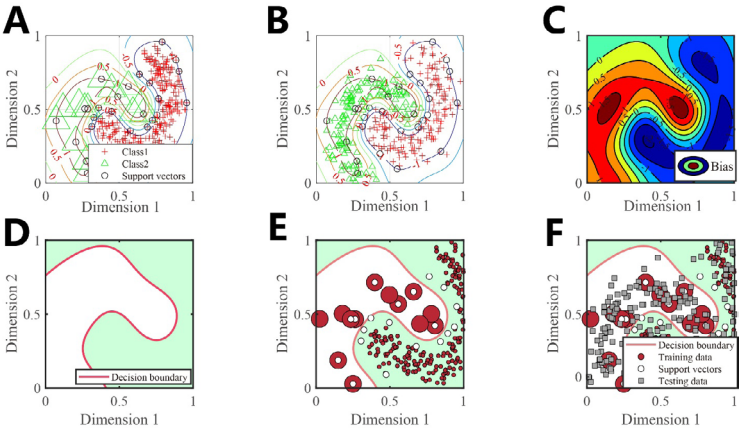


Figure 7. Classification results of the weighted support vector machine (w-SVM) classifier on an imbalanced dataset. (A) Training set and corresponding support vectors. (B) Test set. (C) Bias contour. (D) Decision boundary of the SVM classifier. (E) Support vectors, decision boundary, and training set. (F) Support vectors, decision boundary, training set, and test set. Different point shapes denote distinct classes, and their sizes indicate the corresponding trade-off parameter w_1 used during training.

2.2.3. Adaptive optimization of parameters

After mixing in abundant virtual samples, the rebuilt S may still suffer from another imbalance issue due to the volume gap between $\boldsymbol{S}^{\mathrm{v}}$ and $\boldsymbol{S}^{\mathrm{c}}$. Therefore, to avoid the classifier being overly affected by any data source, either core or modeling, we used $\boldsymbol{w}_2$ to assign the weight between $\boldsymbol{S}^{\mathrm{c}}$ and $\boldsymbol{S}^{\mathrm{v}}$. If using a constant source weight h here, the optimal hyperparameter h^* is determined via K-fold cross-validation grid search over a predefined candidate set (**Equation 8**):

$$\hat{\boldsymbol{\theta}}(h^*) = \arg\min_{\boldsymbol{\theta}} \mathcal{L}(\boldsymbol{\theta}; h)$$
$$\mathcal{L}(\boldsymbol{\theta}; h) = -\frac{1}{N_{\text{train}}} \sum_{n=1}^{N_{\text{train}}} w_1^{(n)} \cdot w_2^{(n)}(h) \cdot \log \hat{p}_{\boldsymbol{\theta}}\left(y^{(n)} | \boldsymbol{x}^{(n)}\right) \quad (8)$$

where $\hat{\boldsymbol{\theta}}(h)$ represents the optimal parameters obtained by training under a given h value, $\hat{p}_{\boldsymbol{\theta}}\left(y^{(n)} \boldsymbol{x}^{(n)}\right)$ denotes the predicted probability of the ground-truth class for the n-th sample, output by the classifier with parameters θ, and L is the weighted cross-entropy loss computed on the training set.

Data-source weight w_2 assigns a tunable coefficient h to real core samples and a fixed baseline weight of 1 to virtual samples (**Equation 9**):

$$w_2^{(n)}(h) = h \cdot 1\left(n \in \boldsymbol{S}^{\mathrm{c}}\right) + 1\left(n \in \boldsymbol{S}^{\mathrm{v}}\right) \quad (9)$$

As shown in Figure 8, cores are split into multiple subsections, each of which is used as the test set in turn, while the remaining subsections are mixed with virtual samples to form the training set. The undetermined parameters of w-SVM, including C, γ, and h, are optimized by minimizing the prediction error from cross-validation. Following the suggestions of *Yuan and Wang*, we adopt particle swarm optimization (PSO) as the global optimizer to solve **Equation 8,** which balances search accuracy and efficiency.[31] After convergence, we substitute the optimal h^* into **Equation 9** to obtain the data-source weight vector $\boldsymbol{w}_2$.

Figure 9 illustrates the construction steps of a pore structure classifier with a dual trade-off. First, the rock properties ($\boldsymbol{m}^{\mathrm{c}}$ and $\boldsymbol{x}^{\mathrm{c}}$) of core samples ($\boldsymbol{S}^{\mathrm{c}}$) are measured under laboratory conditions. Second, w_1 is calculated from core labels ($\boldsymbol{y}^{\mathrm{c}}$), the virtual set ($\boldsymbol{S}^{\mathrm{v}}$) with random physical properties ($\boldsymbol{m}^{\mathrm{v}}$) is generated through the VSG procedure, and its elastic response ($\boldsymbol{x}^{\mathrm{v}}$ is calculated using the fast DEM approach. The training set is built by combining S^{c} and S^{v}. Third, output $\boldsymbol{w}_2$ and other hyper-parameters from PSO search results. Fourth, generalize this well-trained classifier to obtain pore structures of unknown samples.

This approach ensures computational efficiency by eliminating the need to invert for parameters such as porosity and lithology, and the learning process is inherently self-adaptive. For instance, when processing non-defective data, the scheme can degenerate into an unweighted scheme to reduce computational overhead.

3. Results

In this section, the proposed classifier and baseline classifiers were tested for their accuracy and robustness on tasks of both laboratory-scale and logging-scale generalization for pore structure characterization of carbonate rocks.

3.1. Laboratory-scale generalization

3.1.1. Data preparation

Under laboratory conditions, core plugs of carbonate rocks drilled from adjacent boreholes were used to compare their generalized labels with observed structures. Core rock-physics parameters, including mineral volume fraction, pore structure, total porosity, and elastic properties, were measured via X-ray diffraction, micro-CT imaging, helium porosimetry, and in-situ ultrasonic transmission measurement, respectively. The detailed experimental parameters and their corresponding measured values are summarized in Table 1. As shown in Figure 10, we developed a theoretical model for gas-saturated carbonate rocks using the fast DEM approach, with mineralogical parameters following Li *et al.*[24] The agreement rate between predicted (curves) and measured (circles) velocities achieved 93%, and the regression coefficient (R^2) exceeded 85%.

The classification results of pore structures, distinguished by different colors in the figure, show that cracked samples (marked black) are tighter and more compliant, while porous samples (marked white) show the opposite trend.

The raw dataset exhibited severe class imbalance in terms of data quality, as quantified by the IR. This issue originated from the challenges associated with coring and sample preparation for brittle porous rock materials. As shown in Figure 11, to compare the robustness of different pore structure classifiers under such data defectiveness, a subset of 50 samples split out from the raw set was used as the test set to evaluate classifiers trained on: (i) 24 unweighted cores, (ii) 100 unweighted virtual samples, (iii) 100 unweighted hybrid samples, and (iv) 100 weighted hybrid samples. The three-dimensional feature space consisted of normalized density, P-wave velocity, and S-wave velocity.

To enhance the data distribution range and density, the hybrid dataset (Figure 11C) was constructed by mixing

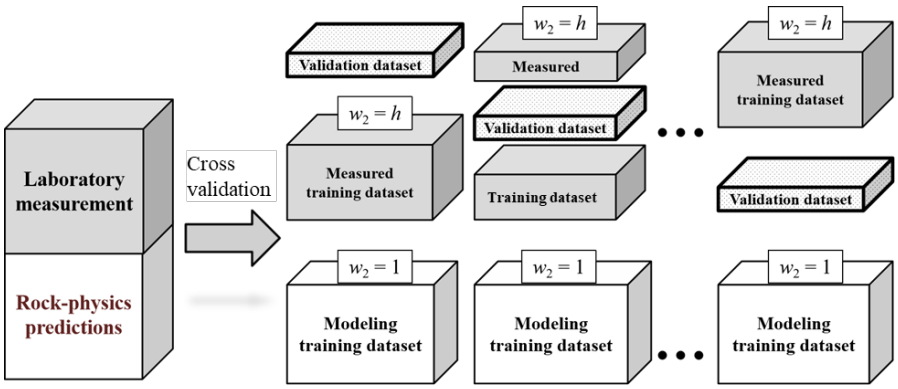


Figure 8. Cross-validation sketch of the adaptive weighting scheme based on the data-model hybrid training dataset. Gray cubes represent core measurements of rock-physics parameters, while white cubes denote virtual samples generated by the virtual sample generation and fast differential effective medium procedures.

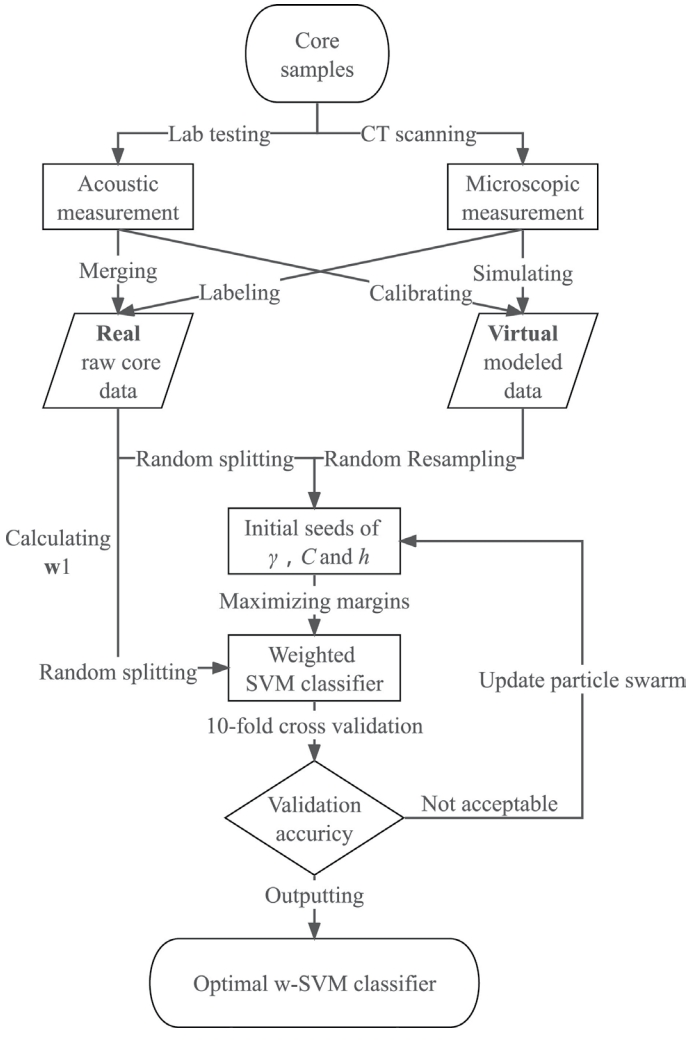


Figure 9. The workflow for the proposed carbonate pore structure classifier with a dual trade-off
Abbreviations: CT: Computed tomography; SVM: Support vector machine; w-SVM: Weighted variant of the support vector machine.

Table 1. The rock-physics parameters involved in this test, as well as their corresponding physical implications, mathematical symbols, representative elements, and measurement methods

Property	Symbol	Elements	Measurements
Mineral fraction	f	Dolomite, calcite, and clay.	The X-ray diffraction method.
Aspect ratio	α	Microcracks, interparticle pores, and vuggy pores.	The ellipse detection method for computed tomography images, as shown in Figure 1.
Pore fraction	v		
Pore volume	φ	Total effective porosity.	The helium volume method.
Elastic property	X	Acoustic wave velocity; shear wave velocity; bulk density.	The transducer emits 500 kHz vibrations under a 55 MPa confining pressure; weight and volume measurement.

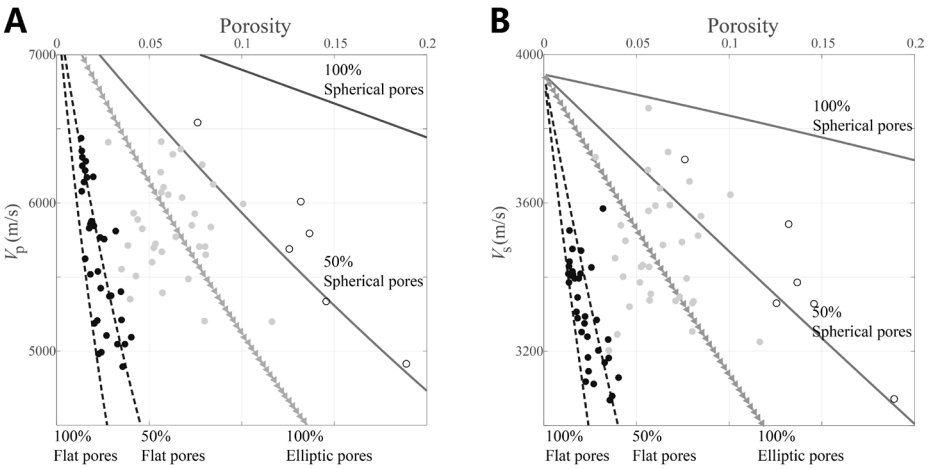


Figure 10. The crossplot of porosity versus modeled (curves) and measured (circles) velocities for (a) P-wave and (b) S-wave. The colors of the circles represent the pore structure labels of carbonate rock samples. The regression coefficients (R^2) of the fast DEM model are 0.866 and 0.891 for P-wave and S-wave velocities, respectively.

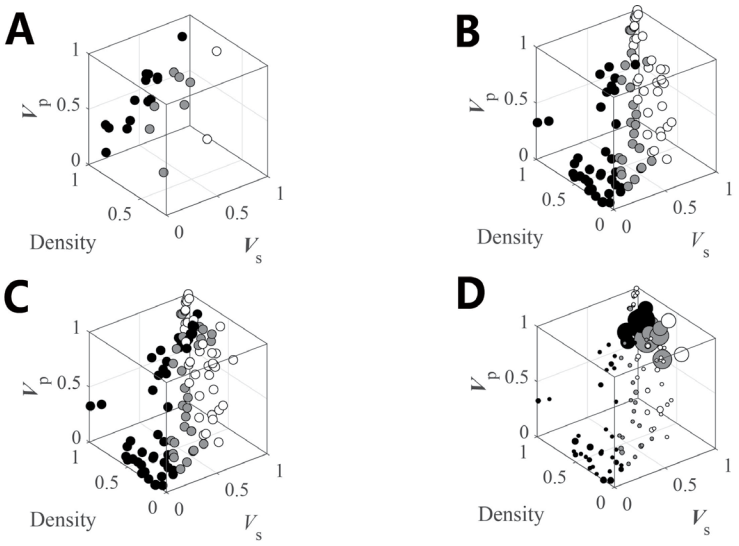


Figure 11. The training set (circles) distribution in the three-dimensional feature space, consisting of normalized density, P-wave velocity, and S-wave velocity. Candidate pore structure classifiers are independently trained on: (A) Unweighted 24 cores, (B) unweighted 100 virtual samples, (C) unweighted 100 hybrid samples, and (D) weighted 100 hybrid samples. The colors of the circles represent the pore structure labels, and the sizes indicate their weights in training.

real samples (Figure 11A) and virtual samples (Figure 11B) through repeated VSG and fast DEM procedures. This construction process reduced the IR and SR of the original dataset from 7.5 and 2.0 to 1.6 and 0.5, respectively, indicating that the proposed method effectively improved data quality. On this basis, the dual trade-off scheme (Figure 11D) prioritized matching minority samples and real core samples during the model training process, which was distinct from the unweighted approach (Figure 11C). Thereafter, these data sets were fed to corresponding w-SVM models to optimize hyperparameters using a PSO algorithm. 10-fold cross-validation yields a final training accuracy of 98% and an optimal hyperparameter vector [γ, C, h] = [5.6, 1.6, 6.7].

3.1.2. Accuracy analysis

Figure 12 presents the scatter plots of the classification results obtained after the first round of data splitting, and Figure 13 shows the histogram of the average label distribution across ten repeated data splitting runs. Classifier A failed to identify any Class #3 samples because of the extremely low proportion of such samples in the core dataset (Figures 12A and 13A). Similarly, classifier B misclassified many Class #1 samples because rock-physics models are highly sensitive to parameter fluctuations (Figures 12B and 13B). Although adopting the hybrid dataset in classifier C yielded a minor performance improvement (Figures 12C and 13C), the classifier remained misled by the majority class and showed clear classification bias. As illustrated in Figures 12D and 13D, classifier D increased the recognition accuracy of classifier C by 25%, and the resulting trade-off effectively improved the robustness of the classification model.

Mechanistically, the main reason for the above differences is that the classification performance of unweighted classifiers is highly susceptible to the label distribution of training samples. Accordingly, classifier A exhibited substantially poorer performance on minority labels #2 and #3 compared to samples of label #1. For classifiers B and C, trained on datasets extended with virtual samples generated from inherent rock-physics rules, this class imbalance is mitigated to some degree. Nevertheless, such minority-class compensation is aimless and may even introduce spurious features absent from the original data, thus misleading the classifier. In contrast, the weighted classifier enables virtual samples to adjust their importance according to the real label distribution, and thus guides classifier D to adaptively yield more reasonable predictions.

3.1.3. Statistical significance analysis

To statistically verify whether the accuracy increment from the proposed classifier is non-random (i.e., statistically meaningful), a repeated random sampling protocol paired with McNemar's test was established.[26] The sample pool comprises 255 cores of carbonate rocks drilled from a wider range of wells. In each iteration, 100 samples were randomly selected without replacement from the pool, of which 30 samples were randomly allocated to the training set for classifier (A–D) training, and the remaining 70 samples served as the test set, whose predictive results were used for pairwise comparisons. The iteration was independently repeated five times, and the pooled continuity-corrected statistic (χ^2) and p-value (p) were calculated to confirm the statistical significance of performance differences between classifiers.

The pairwise McNemar's tests conducted between the classifier D and baseline classifiers (A–C) are summarized in Table 2. Results are reported for each of the pore structure labels (#1, #2, #3) and across all labels. In general, all three pairwise comparisons achieved statistical significance at the 0.05 level. The classifier D delivered highly significant performance compared to classifiers (A–C), with overall corrected χ^2 values always exceeding 8.00 and p-values less than 0.05. Label-wise analysis further confirmed the advantage of classifier D for the minority pore structure classes #2 and #3. The corrected χ^2 values range from 8.00 to 9.00 for Class #2 and from 4.00 to 11.00 for Class #3, with p-values consistently below 0.05 across the three baselines, indicating that the observed performance gains in **Section 3.1.1** are statistically robust and not attributable to random sampling variation.

3.2. Logging-scale generalization

3.2.1. Data preparation

The proposed approach was applied to logging data as an example of cross-scale generalization. The target carbonate interval is saturated by gas and water, with a thickness of 100 m and a sampling rate of 0.05 m. From top to bottom, lithological subzones are defined: Sub-Layer #1 of limestone-dolomite mixture, limestone-rich Sub-Layer #2, and dolomite-rich Sub-Layer #3.

The 105 cores drilled from this well log, with a natural pore structure label distribution of 4:2:1 for Class #1, #2, and #3, were randomly split into a training subset (S^c) and a checkpoint subset (C^c) at an approximate 4:1 ratio under stratified constraints, and this process was repeated three times. The checkpoint subset consisted of 20% of real cores (21 samples) drawn from the total pool in each independent run and unused in the previous classifier training. A stratified sampling strategy was employed to ensure a balanced label distribution in pore structure proportion within the checkpoint subsets (seven samples

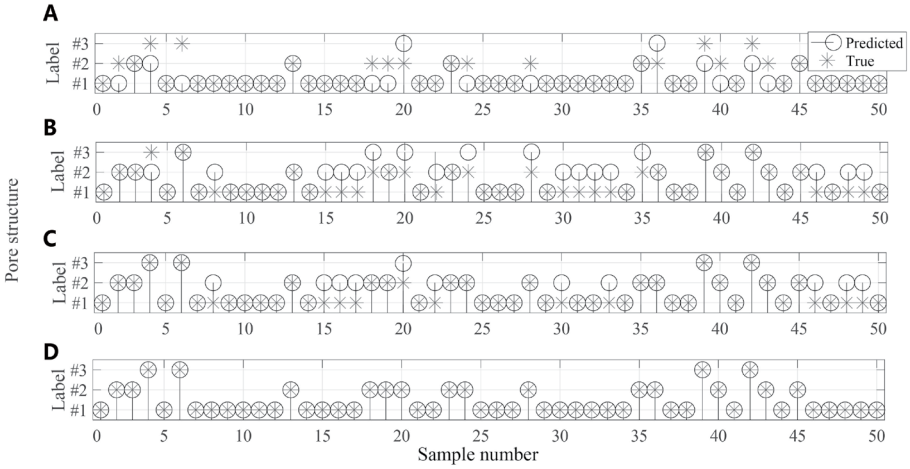


Figure 12. Scatter plot of true (star) and predicted (circle) pore structures for 50 test samples obtained after the first round of data splitting. Candidate classifiers are independently trained on: (A) Unweighted 24 cores, (B) unweighted 100 virtual samples, (C) unweighted 100 hybrid samples, and (D) weighted 100 hybrid samples.

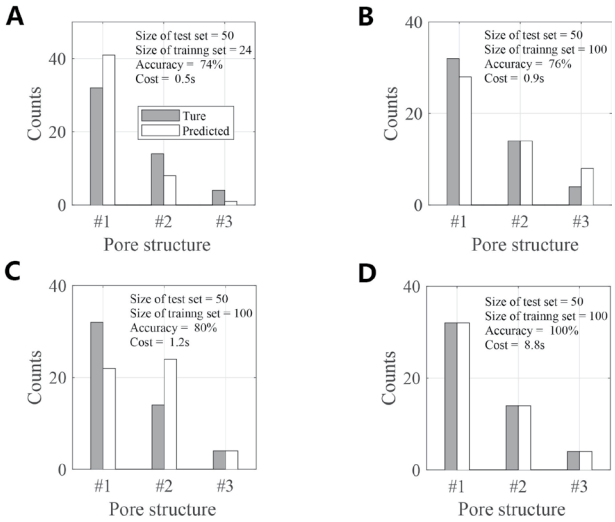


Figure 13. Histogram of the label distribution of true (gray) and predicted (white) pore structures (averaged over ten repeated data splitting runs). In each run, candidate classifiers are independently trained on: (A) Unweighted 24 cores, (B) unweighted 100 virtual samples, (C) unweighted 100 hybrid samples, and (D) weighted 100 hybrid samples.

Table 2. Pairwise continuity-corrected McNemar's test[a] across classifiers

Pairwise Comparison	Corrected χ^2		*p*-value		Significant ($p < 0.05$)
Classifier A vs. D	Overall: 12.071	#1: 6.125; #2: 9.091; #3: 10.828	Overall: < 0.001	#1: 0.013; #2: 0.003; #3: 0.003	Yes
Classifier B vs. D	Overall: 11.077	#1: 10.083; #2: 10.083; #3: 6.125	Overall: < 0.001	#1: 0.002; #2: 0.002; #3: 0.013	Yes
Classifier C vs. D	Overall: 8.100	#1: 7.111; #2: 8.100; #3: 4.167	Overall: 0.004	#1: 0.008; #2: 0.004; #3: 0.041	Yes

Notes: [a]The continuity-corrected χ^2 statistic quantifies the deviation between the observed counts of discordant paired predictions and the distribution expected under the null hypothesis of equal classifier performance, while the *p*-value represents the probability of observing a χ^2 statistic at least as extreme as the calculated value if the two classifiers had no true performance difference; in general, a larger χ^2 value indicates a more substantial performance gap between the compared models, and a smaller *p*-value provides stronger statistical confidence that the observed difference is not due to random chance.[26]

for each of Class #1, #2, and #3) and a reasonable spatial distribution that spanned all depth ranges and lithofacies of the study area (one or two samples every 10 m).

As shown in Table 3, each training subset was used to construct four candidate classifiers, following the procedures in **Section 3.1**, while the corresponding checkpoint subset was used to evaluate these classifiers. As the test set was drawn from unlabeled logging curves, the measure of classifier performance was defined as the consistency ratio between pore structure labels derived from core checkpoint observations and those obtained from corresponding logging predictions within the depth domain. Notably, the PSO hyperparameter search range was predefined based on suggestions from Yuan and Wang,[31] trial experiments, and the physical interpretability of carbonate pore classification. For the RBF kernel parameter γ, the lower bound of 0.1 avoided overly linear classification boundaries, while the upper bound of 100 prevented severe overfitting to training noise. For the SVM penalty coefficient C, the range [0.1, 100] balanced the risk of underfitting from small penalty values and the risk of overfitting from excessively large penalties. With regard to the source weight h, a lower limit of 0.1 ensured that geological information was not neglected, and an upper limit of 10 maintained the imbalance-correction effect of the massive virtual sample set.

The pore fluid was gas and brine, whose saturation information had already been inverted from the resistivity logging curves and Archie's formulas.[24] Based on the statistical equivalence principle of multiscale acoustic data proposed by Bailly *et al.*,[27] a consistency correction was employed to integrate data obtained under logging (500 kHz) and laboratory conditions (54 kHz). As shown in **Equation 10**, elastic moduli K and G of the core scale (superscript c) can be upscaled to the logging scale (superscript l) using measured Poisson ratio ν and logging density curves ρ (**Equation 10**):

$$\frac{K^{\mathrm{l}}}{K^{\mathrm{c}}}=\frac{(1-2\nu)e^{-16\rho^{\mathrm{l}}/9}}{1-2\nu e^{-8\rho^{\mathrm{l}}/5}},\qquad \frac{G^{\mathrm{l}}}{G^{\mathrm{c}}}=\frac{(1+\nu)e^{-16\rho^{\mathrm{l}}/9}}{1+\nu e^{-8\rho^{\mathrm{l}}/5}}, \tag{10}$$

By doing so, the coincidence rate between different scaled data improves from 77.1% to 93.2%. The test set was encoded from density and acoustic logging curves. The fluid and mineralogy inputs in the DEM model were abstracted from radioactivity and resistivity logging statistics. As shown in Figure 14A and 14B, the hybrid set reduced the IR and SR of the core set from 7.8 and 25.6 to 1.2 and 4.0. The trade-off w (point sizes in Figure 14B) was derived from the optimized hyperparameters of [γ, C, h] = [25.6, 24.7, 1.2]. This optimal parameter combination delivered stable performance. Within ± 50% fluctuation around each optimal value, the macro-F1 score varied by less than 2.1%, and the generalized result achieved a validation rate of 99.1% (Figure 14C).

3.2.2. Result analysis

As shown in Table 4, after three rounds of drawing, splitting, training, and generalization, the classification accuracy of the four listed classifiers was calculated and compared. Both overall and per-class accuracies were computed on this unified pooled checkpoint set. The continuity-corrected McNamara's test was again adopted to statistically examine the performance difference between each baseline classifier and the proposed weighted hybrid classifier D. The significance threshold was set at $\alpha = 0.05$ for all tests.

The inherent class imbalance of core labels (4:2:1 ratio) underlay the performance gaps among the three baseline strategies. Classifier A, trained exclusively on real core data, achieved a 57.1% overall accuracy but tended to favor the majority Class #1 to reduce overall classification loss, which sacrificed the accuracy of the minority Class #3. Classifier B alleviated class imbalance by supplementing virtual samples, achieving a 71.4% overall accuracy, but it lacked support from real geological information. On this basis, classifier C integrated real and virtual samples and achieved a 79.3% overall accuracy. However, it did not balance the contributions of sources and labels, leading to unstable prediction results. The proposed weighted hybrid classifier D resolved the trade-off among data authenticity, class balance, and training stability, yielding the highest overall accuracy (96.8%) and outperforming all baselines across every individual class. The continuity-corrected McNemar's test confirmed that these performance advantages were statistically significant ($p < 0.05$) at both the overall and per-class levels. In particular, the improvement for the minority class (Class #3) was consistently significant across all baseline comparisons.[26] Some comparisons involving Class #1 and #2 did not reach statistical significance, mainly due to the smaller number of discordant prediction pairs and relatively high baseline performance.

3.2.3. Geophysical and geological implications

From the perspective of regional geology, the vertical pore structure heterogeneity (Figure 15) reflects the integrated evolution of regional dolomitization, burial compaction, and multi-stage tectonic stress. Sub-layer #1 consisted of interbedded limestone and dolomite, experiencing superimposed diagenetic modifications:

Table 3. Data and classifier parameters involved in this test

Parameter	Data		Classifier	
	Training data	Test data		
Size	500 × (3 + 1)	2,000 × 3	Method	w-SVM
Attributes	$[V_p, V_s, \rho]$	$[V_p, V_s, \rho]$	Fold	10
Source	Laboratory: Elastic measurements / Modeling: Fast DEM predictions	Acoustic logging curves; shear wave logging curves; density logging curves	Optimizer	PSO
			Min γ, C, h^a	[0.1, 0.1, 0.1]
			Max γ, C, h^a	[100, 100, 10]
			Swarm size	30

Notes: [a]The lower and upper bounds of the hyperparameters are determined via joint consideration of pre-experimental screening, published research results, and constraints from geological interpretability.
Abbreviations: DEM: Differential effective medium; w-SVM: Weighted variant of the support vector machine.

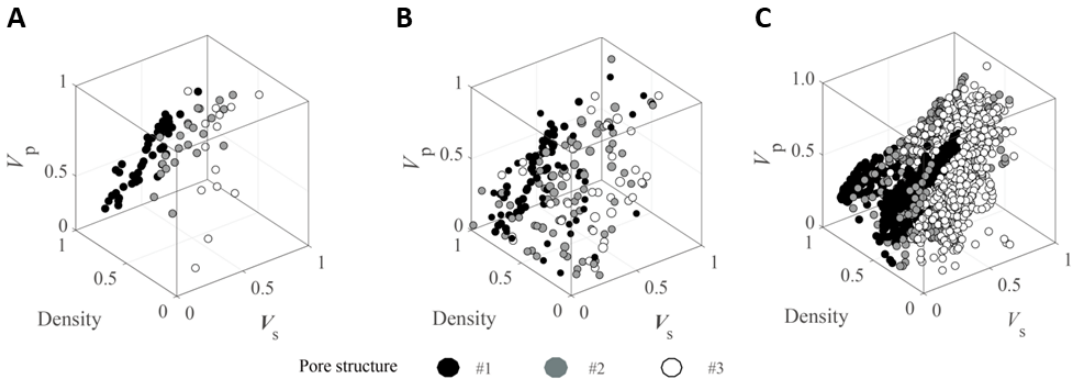


Figure 14. Scatter plot of sample distribution (circles) in the three-dimensional feature space, consisting of normalized density, P-wave velocity, and S-wave velocity for (A) raw core set, (B) rebuilt hybrid set with the dual trade-off, and (C) generalized logging data. The colors of the circles represent the pore structure labels, and the sizes indicate their weights in training.

Table 4. Overall and per-class performance of the candidate classifier evaluated on the pooled checkpoint set

Classifier			Pooled accuracy (%)				Pooled continuity-corrected McNemar's test (vs. D), $\alpha = 0.05$			
No.	Data	Weighted	Overall	Class #1	Class #2	Class #3	Overall	Class #1	Class #2	Class #3
A	Core	No	57.1	71.4	52.4	47.6	$\chi^2 = 13.9$, $p = 0.001$	$\chi^2 = 1.3$, $p > \alpha$	$\chi^2 = 7.1$, $p < \alpha$	$\chi^2 = 9.1$, $p < \alpha$
B	Model	No	71.4	80.9	76.2	57.1	$\chi^2 = 7.7$, $p = 0.005$	$\chi^2 = 1.1$, $p > \alpha$	$\chi^2 = 3.2$, $p > \alpha$	$\chi^2 = 8.4$, $p < \alpha$
C	Hybrid	No	79.3	85.7	85.7	66.7	$\chi^2 = 6.7$, $p = 0.009$	$\chi^2 = 0.8$, $p > \alpha$	$\chi^2 = 1.8$, $p > \alpha$	$\chi^2 = 5.1$, $p < \alpha$
D	Hybrid	Yes	96.8	95.2	95.2	100.0	–	–	–	–

Notes: All numerical results were retained to two decimal places; the notation $p < \alpha$ indicates that a statistically significant difference exists between the candidate classifier and the baseline classifier D.[26]

early dolomitization generated intercrystalline elliptical pores, extensional tectonic events created directional microcracks (flat pores), and meteoric freshwater dissolution produced isolated spherical vugs, resulting in coexisting pore populations with strong vertical heterogeneity. Sub-layer #2 was dominated by limestone lithology; intense mechanical compaction during shallow burial largely eliminated primary intergranular pores, while regional compressional paleostress fractured the brittle limestone matrix and formed pervasive flat microcracks, with negligible vug development due to weak dolomitization and limited fluid-rock dissolution. Sub-layer #3 underwent early complete dolomitization, which greatly enhanced matrix mechanical rigidity and mitigated compaction damage to primary pore space. Subsequent deep-burial organic acid dissolution formed abundant moldic and intracrystalline spherical vugs, and the stable weak-stress tectonic background avoided large-scale fracture compaction.

From the perspective of geophysical reservoir division, dolomitized intervals with moderate burial dissolution and low tectonic compression (Sub-layer #3) host dominant vuggy pores and represent favorable high-quality reservoir intervals, whereas fracture-dominated limestone layers (Sub-layer #2) exhibit poor storage capacity despite high crack density. This pore structure characterization provides direct geological constraints for predicting favorable carbonate reservoir zones in the study area. As shown in Figure 16, the cracked carbonate zones were characterized by low velocity and high density, whereas the porous zones exhibited the opposite characteristics (Figure 16A–16C). As a conventional reserve indicator, rock porosity appeared to follow a structure-dependent normal distribution, with means of 0.02, 0.03, and 0.09 for zones dominated by Classes #1, #2, and #3, respectively (Figure 16D). Thus, from an interpretation perspective, Class #3 intervals may indicate optimal storage conditions, while Class #1 intervals may correspond to risky exploration targets.

4. Discussion

4.1. Uncertainties

As illustrated in Figure 10, the calculated coefficients of determination indicate that the fast DEM model explained more than 87% of the overall velocity variation pattern of the carbonate samples, confirming that porosity and pore geometry are the dominant controlling factors of elastic wave velocity. The remaining unexplained variance is jointly driven by two categories of uncertainties: modeling uncertainty and data uncertainty.

4.1.1. Modeling uncertainty

Modeling uncertainty may stem from theoretical simplifications and preset assumptions embedded in the fast DEM forward-modeling framework, which determines the upper limit of fitting consistency between modeled and real rock elastic responses. Following Lucia,[18] all natural carbonate pore subtypes are aggregated into flat, elliptical, and spherical pores only by aspect ratio. This ignores mixed multiscale pore superposition in real cores (e.g., coexistence of microcracks and vugs with variable mixing ratios), leading to fixed systematic bias for samples with complex composite pore assemblages.[12,21] This simplification explains why a small portion of the measured points deviate from the theoretical curves, and is the primary contributor to the imperfect R^2 of less than 0.9 in Figure 10.

4.1.2. Measurement uncertainty

Measurement uncertainty arises from laboratory testing, micro-CT pore characterization, and logging data preprocessing, producing random scattered deviations of measured velocity points relative to the theoretical trend, including random noise in acoustic measurements, errors in pore parameter measurements from micro-CT scanning and pixel segmentation, and the residual of cross-scale data consistency correction.[32,33]

4.2. Sensitivities

To quantitatively evaluate the impact of rock-physics model simplifications on classification performance and verify the robustness of the proposed dual-trade-off framework, we conducted two groups of systematic sensitivity tests.

4.2.1. Parameter perturbation

This study employed perturbation tests to investigate the sensitivity of the proposed pore structure classifier to input parameter perturbations. Perturbed inputs (m^{v*}) were obtained by introducing controlled graded relative errors into the parameters of virtual samples (m^{v}) generated from the VSG procedure. Three levels of relative error (±10%, ±20%, ±30%) were introduced separately into pore geometry α, pore composition v, mineral composition f, and total porosity φ. The real pore structure labels y^{v} were then compared with the classification outputs predicted by the proposed classifier trained on the perturbed inputs $g(m^{v*})$.

Quantitative analysis results show that, among all the investigated parameter categories, the aspect ratio contributed the largest proportion of the total accuracy fluctuation of the classifier, followed by pore component volume fractions. In comparison, mineral component fractions and total porosity exerted relatively mild influences on accuracy, accounting for approximately 10% and 5% of the total fluctuation, respectively. For

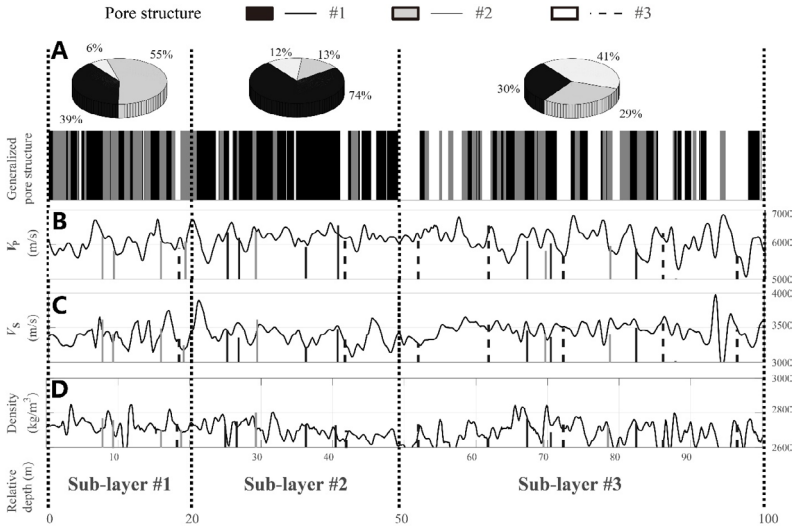


Figure 15. The generalized pore structure of logging data, where (A) represents the label distributions (colors) within different subzones, generalized from the feature space comprising (B) P-wave velocity, (C) S-wave velocity, and (D) density. Stems are checkpoints whose colors and lengths correspond to their real measured labels and elastic properties, respectively.

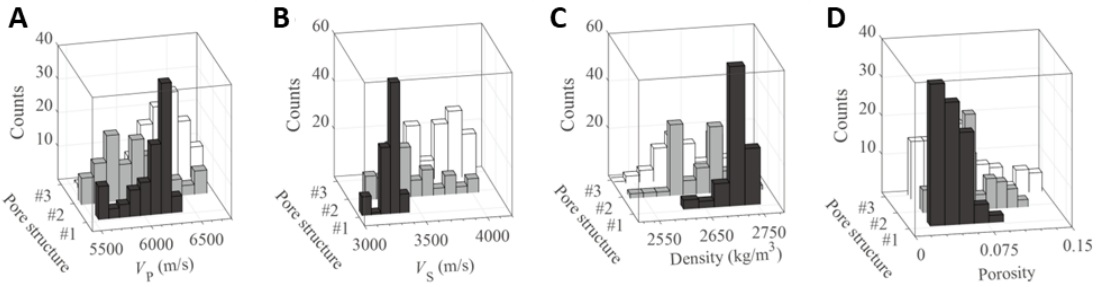


Figure 16. Histogram plot of the rock properties versus pore structures, including (A) P-wave velocity, (B) S-wave velocity, (C) density, and (D) porosity

core rock-physics input parameters, when the relative perturbation was constrained within ± 30%, which is the geologically reasonable range for carbonate reservoir parameters, the overall classification accuracy of the model was maintained within a fluctuation margin of ± 5.2%. Specifically, the accuracy fluctuation was 1.2% under the ± 10% perturbation level, 2.8% under ± 20%, and 5.2% under ± 30%. Furthermore, the maximum accuracy fluctuation of any single class did not exceed ± 7.1%. This confirms that the core conclusions of this study are robust and not sensitive to measurement errors in the rock-physics model inputs.

4.2.2. Pore system complexity

Degradation experiments were further conducted to verify whether the simplification of the three-endmember pore system imposed constraints on the adaptive capacity of the model for naturally complex pore systems. To incorporate the natural intra-class heterogeneity of pore geometries, the actual rock-physics parameters (m^{v**}) were reconstructed by expanding the input dimension of pore components (α and v) from three discrete components to 12 discrete components. For each of the original three endmembers, 1–4 discrete values were sampled from a normal distribution with the original value as the mean and a relative standard deviation of 15%, and the corresponding volume fractions were sampled from a Dirichlet distribution under the constraint that the sum of all volume fractions equals 1. Finally, the true label y^{v**} was compared to the predicted result y^{v} obtained from the classifier trained on the three-endmember pore system input $g(m^{v})$.

Quantitative analysis results show that when the number of pore components increased from 3 to 12, the overall classification accuracy of the model decreased by an average of 2.7%, and a maximum accuracy reduction of

3.5% was recorded in multiple repeated experiments. Such accuracy degradation is mainly attributed to the increased overlap of elastic responses between adjacent pore types, which is an inherent property of refined multi-component pore systems. This result indicates that the proposed classifier effectively captures the elastic response patterns corresponding to dominant pore structures, rather than undergoing overfitting to specific fixed aspect ratio values. Thus, when the pore system is discretized into a greater number of components, the characterization results still maintain stable generalization performance and remain insensitive to reasonable parameter simplification operations.

4.3. Limitations

4.3.1. Applicable field

Admittedly, the current implementation of the proposed scheme has clear application boundaries. First, it relies on multiple data sources and requires systematic laboratory measurements and cross-scale consistency correction in advance; alternative strategies for data-deficient scenarios should be explored in future work. Additionally, the current rock physics model, pore structure classification system, and feature space are calibrated specifically for carbonate reservoirs.[34] Direct application without the above recalibration may lead to notable degradation in prediction performance and unreliable geological interpretation.

4.3.2. Robustness

Although four training strategies with single weighted/unweighted SVM were compared in this study, the absence of a multi-classifier ensemble and fusion architecture is a potential robustness limitation. As indicated in Woods *et al.*,[35] dynamic classifier selection can match the optimal base model for regional feature clusters, while fuzzy integral fusion can non-linearly integrate complementary output information from multiple base models such as support vector machine, random forest, and K-nearest neighbor. Without these modules, the current identification scheme may struggle to recognize minority spherical vug pore samples.[36]

4.4. Potential improvements

Firstly, the core methodological framework can be extended to other reservoir types, including tight sandstone, volcanic, and shale reservoirs, to enable pore structure characterization under non-ideal data scenarios. Prior to adapting the proposed method to new lithologies, the following recalibration procedures are required: (i) Reconstruct the pore geometry classification system based on core thin-section observations and scanning electron microscope imaging data from the target formation to match the local pore-structure characteristics and diagenetic origins of the study area. (ii) Recalibrate the mineral matrix parameters, pore fluid parameters, and pore structure parameters of the rock-physics forward model based on regional rock-physics rules and local core measurement data.[17,18] (iii) Retune the hyperparameters of data source weights using cross-validation based on local labeled core samples, so as to adapt to the differences in data distribution between different formations.[19]

Secondly, a multi-classifier ensemble and adaptive fusion framework should be constructed to enhance the robustness of the identification results, which includes: (i) Weighted Bagging ensemble: A base learner pool can be constructed, which consists of the dual-trade-off weighted SVM, weighted random forest, and weighted K-nearest neighbor. The bootstrap resampling strategy and majority voting rule are adopted to reduce the prediction variance introduced by the limited size of core samples.[29,31] (ii) AdaBoost boosting ensemble: Taking lightweight weighted SVM as the weak classifier, the loss weights of misclassified minority pore structure samples are iteratively increased to further alleviate the bias caused by data imbalance.[31] (iii) Dynamic classifier selection based on local accuracy: For each test sample, the neighborhood local accuracy of each base model is calculated, and the most reliable classifier is dynamically selected for regional elastic feature clusters.[35] (iv) Fuzzy integral fusion: The posterior probability outputs of multiple base learners are integrated through fuzzy measures to obtain unified pore classification confidence.[36]

5. Conclusion

This study proposes a weighted learning framework for pore structure identification in carbonate rocks. Numerical tests based on measured data demonstrate that: (i) the fast DEM approach employed in this paper is an appropriate rock-physics model that can efficiently and accurately correlate the physical properties of carbonate rocks with their elastic responses; (ii) the proposed dual trade-off strategy can rebalance different sample classes and sample sources, thereby reducing corresponding training biases during model training, which has not been addressed in existing studies; (iii) the adaptive weighted classifier trained on the hybrid dataset that integrates core samples and model-generated samples outperforms both unweighted classifiers and classifiers trained on pure core datasets and pure model-oriented datasets in both accuracy and robustness, and this advantage is particularly pronounced for minority pore structure labels; (iv) even at the well logging scale, the proposed framework can help detect heterogeneous carbonate pore structures, enabling accurate reserve estimation and providing critical insights for inferring geological history from logging data.

Acknowledgments

None.

Funding

The present study was supported by the Scientific Research Program of the Jiangsu Education Department (Grant No. 20KJB170005) and Hebei Natural Science Foundation (Grant No. D2026512046).

Conflict of interest

The authors declare that they have no competing interests.

Author contributions

Conceptualization: Bonan Li
Data curation: All authors
Investigation: All authors
Methodology: Bonan Li
Resources: Bonan Li, Feng Zhu
Writing–original draft: Bonan Li
Writing–review & editing: All authors

Availability of data

Data associated with this research are available from the corresponding author upon reasonable request.

References

1. Weger RJ, Eberli GP, Baechle GT, Massaferro JL, Sun YF. Quantification of pore structure and its effect on sonic velocity and permeability in carbonates. *AAPG Bulletin*. 2009; 93(10):1297-1317.

   doi: 10.1306/05270909001

2. Sun SZ, Wang H, Liu Z, Li Y, Zhou X, Wang Z. The theory and application of DEM-Gassmann rock physics model for complex carbonate reservoirs. *Leading Edge*. 2012;31(2):152-158.

   doi: 10.1190/1.3686912

3. Regnet JB, Robion P, David C, Fortin J, Brigaud B, Yven B. Acoustic and reservoir properties of microporous carbonate rocks: Implication of micrite particle size and morphology. *J Geophys Res*. 2015;120(2):790-811.

   doi: 10.1002/2014jb011313

4. Mavko G, Mukerji T, Dvorkin J. *The Rock Physics Handbook*. 2nd ed. Cambridge, United Kingdom: Cambridge University Press; 2009.

   doi: 10.1017/cbo9780511626753

5. Li B, Shen H, Qu S, Wang D, Liu C. Tight carbonate reservoir characterization based on the modified rock physics model. *J Appl Geophys*. 2018;159:374-385.

   doi: 10.1016/j.jappgeo.2018.09.012

6. Fabricius IL, Baechle GT, Eberli GP. Elastic moduli of dry and water-saturated carbonates -Effect of depositional texture, porosity, and permeability. *Geophysics*. 2010;75(3):N65-N78.

   doi: 10.1190/1.3374690

7. Matsushima J, Ali MY, Bouchaala F. Propagation of waves with a wide range of frequencies in digital core samples and dynamic strain anomaly detection: Carbonate rock as a case study. *Geophys J Int*. 2020;224(1):340–354.

   doi: 10.1093/gji/ggaa467

8. Eberli GP, Baechle GT, Anselmetti FS, Incze ML. Factors controlling elastic properties in carbonate sediments and rocks. *Leading Edge*. 2003;22(7):654-660.

   doi: 10.1190/1.1599691

9. Wang Z, Wang R, Weger RJ, Li T, Wang F. Pore-scale modeling of elastic wave propagation in carbonate rocks. *Geophysics*. 2015;80(1):D51–D63.

   doi: 10.1190/GEO2014-0050.1

10. Baechle GT, Colpaert A, Eberli GP, Weger RJ. Effects of microporosity on sonic velocity in carbonate rocks. *Leading Edge*. 2008;27(8):1012-1018.

    doi: 10.1190/1.2967554

11. Jiang L, Wen XT, Zhou DH, He ZH, He XL. The constructing of pore structure factor in carbonate rocks and the inversion of reservoir parameters. *Appl Geophys*. 2012;9(2):223-232.

    doi: 10.1007/s11770-012-0333-5

12. Sayers CM. The elastic properties of carbonates. *Leading Edge*. 2008;27(8):1020-1024.

    doi: 10.1190/1.2967555

13. Keys RG, Xu S. An approximation for the Xu-White velocity model. *Geophysics*. 2002;67(5):1406-1414.

    doi: 10.1190/1.1512786

14. Sun YF. Pore structure effects on elastic wave propagation in rocks: AVO modelling. *J Geophys Eng*. 2004;1(4):268-276.

    doi: 10.1088/1742-2132/1/4/005

15. Dou Q, Sun Y, Sullivan C. Rock-physics-based carbonate pore type characterization and reservoir permeability heterogeneity evaluation, Upper San Andres reservoir, Permian Basin, west Texas. *J Appl Geophys*. 2011;74(1):8-18.

    doi: 10.1016/j.jappgeo.2011.02.010

16. Gohari MSJ, Niri ME, Ghiasi-Freez J. Improving permeability estimation of carbonate rocks using extracted pore network parameters: a gas field case study. *Acta Geophys*.2021;69(2):509-527.

    doi: 10.1007/s11600-021-00563-z

17. Li T, Wang Z, Wang R, Yu N. Pore type identification in carbonate rocks using convolutional neural network based on acoustic logging data. *Neural Comput & Applic*.

2021;33(9):4151–4163.

doi: 10.1007/s00521-020-05246-2

18. Lucia FJ. *Carbonate reservoir characterization: an integrated approach*. 2nd ed. Berlin, Germany: Springer-Verla; 2007:29-67.

doi: 10.1007/978-3-540-72742-2

19. Radwan AE, Trippetta F, Kassem AA, Kania M. Multiscale characterization of unconventional tight carbonate reservoir: Insights from October oil filed, Gulf of Suez rift basin, Egypt. *J. Petro. Sci. Eng.* 2021;197:107968.

doi: 10.1016/j.petrol.2020.107968

20. Huang Q, Dou Q, Jiang Y, Zhang Q, Sun Y. An integrated approach to quantifying geological controls on carbonate pore types and permeability, Puguang Gas field, China. *Interpretation*. 2017;5(4):T545-T561.

doi: 10.1190/INT-2016-0166.1

21. Xu S, Payne MA. Modeling elastic properties in carbonate rocks. *Leading Edge*. 2009;28(1):66-74.

doi: 10.1190/1.3064148

22. Mollajan A, Memarian H. Rock physics-based carbonate pore type identification using Parzen classifier. *J. Petro. Sci. Eng*. 2016;145:205-212.

doi: 10.1016/j.petrol.2016.03.021

23. Berryman JG, Pride SR, Wang HF. A differential scheme for elastic properties of rocks with dry or saturated cracks. *Geophys J Int*. 2002;151(2):597–611.

doi: 10.1046/j.1365-246X.2002.01801.x

24. Li B, Si W, Shen H, Zhang X. Building the carbonate pore-type classifier for well logging via the blended training dataset. *Acta Geophys*. 2021;69(1):77–94.

doi: 10.1007/s11600-020-00516-y

25. Stadtmuller M. Well logging interpretation methodology for carbonate formation fracture system properties determination. *Acta Geophys*. 2019;67(6):1933-1943.

doi: 10.1007/s11600-019-00351-w

26. Dietterich TG. Approximate statistical tests for comparing supervised classification learning algorithms. *Neural Comput*. 1998;10(7):1895–1923.

doi: 10.1162/089976698300017197

27. Bailly C, Fortin J, Adelinet M, Hamon Y. Upscaling of elastic properties in carbonates: A modeling approach based on a multiscale geophysical data set. *J Geophys Res Solid Earth*. 2019;124(12):13021-13038.

doi: 10.1029/2019JB018391

28. Cortes C, Vapnik V. Support Vector Networks. *Mach Learn*. 1995;20(3):273-297.

doi: 10.1023/A:1022627411411

29. Song C, Alkhalifah T, Waheed UB. Solving the frequency-domain acoustic VTI wave equation using physics-informed neural networks. *Geophys J Int*. 2021;225(2):846–859.

doi: 10.1093/gji/ggab010

30. Zong W, Huang GB, Chen Y. Weighted extreme learning machine for imbalance learning. *Neurocomputing*. 2013;101:229-242.

doi: 10.1016/j.neucom.2012.08.010

31. Yuan S, Wang S, Tian N. Swarm intelligence optimization and its application in geophysical data inversion, *Appl. Geophys*. 2009;6(2):166-174.

doi: 10.1007/s11770-009-0018-x

32. Nur A, Mavko G, Dvorkin J, Galmudi D. Critical porosity, a key to relating physical properties to porosity in rocks. *Leading Edge*. 2000;17(3):878-881.

doi: 10.1190/1.1437977

33. Vanorio T, Mavko G. Laboratory measurements of the acoustic and transport properties of carbonate rocks and their link with the amount of microcrystalline matrix. *Geophysics*. 2011;76(4):E105-E115.

doi: 10.1190/1.3580632

34. Zhao L, Nasser M, Han DH. Quantitative geophysical pore type characterization and geological implications in carbonate reservoir, *Geophys Prospect*. 2013;61(4):827-841.

doi: 10.1111/1365-2478.12043

35. Woods K, Kegelmeyer WP, Bowyer K. Combination of multiple classifiers using local accuracy estimates. *IEEE Trans Pattern Anal Mach Intell*. 1997;19(4):405–410.

doi: 10.1109/34.588027

36. Sharifi J. Intelligent pore type characterization: Improved theory for rock physics modelling, *Geophys Prospect*, 2022;70(5):921-937.

doi: 10.1111/1365-2478.13204

Appendix

Appendix A: Elastic modulus of multi-structured porous medium

If we assume $n = K_m/G_m$ and $m = n(P^{*i} - Q^{*i})$, the polarization factor of the differential effective medium (DEM) (P and Q) can be decomposed into first- and second-order terms (P_0, Q_0 and P_1, Q_1) that depend on n and (m, n).[29] For penny-shaped pores, these parameters satisfy **Equation A1**:

$$P^{*i} - Q^{*i} = -\frac{1}{5} + \frac{K^*/G^*\left(3K^*/G^* + 4\right)}{\pi\alpha\left(3K^*/G^* + 1\right)} - \frac{4\left(3K^*/G^* + 4\right)}{15\pi\alpha\left(3K^*/G^* + 1\right)} - \frac{8\left(3K^*/G^* + 4\right)}{15\pi\alpha\left(3K^*/G^* + 2\right)} \quad \text{(A1)}$$

For drained rock skeletons, the solution of the decoupled DEM model is shown in **Equation A2**:

$$\begin{cases} K_d = K_m(1-\varphi)^{P_0+P_1} e^{P_1\varphi} \\ G_d = G_m(1-\varphi)^{Q_0+Q_1} e^{Q_1\varphi} \end{cases} \quad \text{(A2)}$$

Equation A2 can be further simplified by its first-order terms of Taylor expansions (**Equation A3**):[30]

$$\begin{cases} K_d = K_m(1-\varphi)^{P_0+P_1} e^{P_1\varphi} \approx K_m(1-\varphi)^{P_0} \\ G_d = G_m(1-\varphi)^{Q_0+Q_1} e^{Q_1\varphi} \approx G_m(1-\varphi)^{Q_0} \end{cases} \quad \text{(A3)}$$

Given a material with I pore components, its modulus K^{*i} is derived from its former condition K^{*i-1}, as shown in **Equation A4**:

$$\begin{aligned} K_d^{*i} &= K^{*i-1}(1-v^i\varphi)^{P_0^i+P_1^i} e^{\varphi P_0^i} \\ K_d^{*i} &\approx K^{*i-1}(1-\varphi)^{v^i(P_0^i+P_1^i)} e^{P_0^i} = K_m(1-\varphi)^{\sum_{i=1}^{I} v^i(P_0^i+P_1^i)} e^{\varphi\sum_{i=1}^{I} v^i P_1^i} \end{aligned} \quad \text{(A4)}$$

Similarly, its shear modulus G^{*i} is calculated as follows (**Equation A5**):

$$G_d^{*i} = G_m(1-\varphi)^{\sum_{i=1}^{N} v^i(Q_0^i+Q_1^i)} e^{\varphi\sum_{i=1}^{N} v^i Q_1^i} \quad \text{(A5)}$$

If added to a pore fluid whose bulk modulus is K_f, the saturated rock modulus K and G can be modeled by the Gassmann theory (**Equation A6**):[4,13]

$$\begin{cases} K = K_d + \dfrac{\left(1 - \dfrac{K_d}{K_m}\right)^2}{\dfrac{\varphi}{K_f} + \dfrac{1-\varphi}{K_m} - \dfrac{K_d}{K_m^2}} \\ G = G_d \end{cases} \quad \text{(A6)}$$

Equation A6 can be further extended to the mixture materials of solid-solid and liquid-liquid phases using Voigt–Reuss–Hill and Wood's mixing laws. Equivalent rock density and velocity are modeled by **Equation A7**:[4]

$$\begin{cases} V_P = \sqrt{\dfrac{K + 4/3G}{\rho}} \\ V_S = \sqrt{\dfrac{G}{\rho}} \end{cases}, \quad \rho = \varphi\rho_f + (1-\varphi)\rho_m \quad \text{(A7)}$$

where ρ, ρ_f and ρ_m are the densities of saturated rock, pore fluid, and mineral mixture. They are usually quantified from logging curves and laboratory experiments.[31,32]

Appendix B: Virtual sample generation

In the workflow of virtual sample generation (VSG) for carbonate pore structure classification, a generated virtual sample can be denoted as $S^{v(0)}$, with its physical attribute vector structured as **Equation B1**:

$$m^{v(0)} = [\varphi^{(0)}, f^{(0)}, v^{(0)}, \alpha^{(0)}], \quad \text{(B1)}$$

where the superscript v indicates the virtual sample, and $(\cdot)$ indicates the sequence number of the sample. $\varphi^{(0)}$ is a scalar representing total porosity, vector $f^{(0)} = [f_1^{(0)}, f_2^{(0)}, \ldots, f_L^{(0)}]^T$ is the volumetric fractions of the L lithological categories in the mineral matrix of carbonate rocks, vector $\boldsymbol{v}^{(0)} = [v_1^{(0)}, v_2^{(0)}, \ldots, v_I^{(0)}]^T$ is the volumetric fractions of the I characteristic pore structures, and vector $\boldsymbol{\alpha}^{(0)} = [\alpha_1^{(0)}, \alpha_2^{(0)}, \ldots, \alpha_I^{(0)}]^T$ are their corresponding characteristic aspect ratios. The total dimension of the attribute vector is $D = 1 + L + 2I$. The VSG procedure is implemented in sequential steps.

For each pore structure class k (e.g., #1, #2, #3), a D-dimensional multivariate Gaussian distribution is fitted using all real cores belonging to that class, totaling N_k samples. The mean vector μ_k and covariance matrix Σ_k of class k are estimated from real training samples $\{m_i\}_{i=1}^{n_k}$ (**Equation B2**):

$$\begin{aligned} \boldsymbol{\mu}_k &= \frac{1}{N_k}\sum_{i=1}^{N_k} \boldsymbol{m}_i \\ \boldsymbol{\Sigma}_k &= \frac{1}{N_k - 1}\sum_{i=1}^{N_k} (\boldsymbol{m}_i - \boldsymbol{\mu}_k)(\boldsymbol{m}_i - \boldsymbol{\mu}_k)^T \end{aligned} \quad \text{(B2)}$$

Thus, the empirically derived full covariance matrix preserves the intrinsic correlation structure among rock-physics attributes. Candidate virtual samples are generated by independent random sampling from the fitted class-conditional multivariate Gaussian distribution (**Equation B3**):

$$\boldsymbol{m}^{v(0)} \sim N(\boldsymbol{\mu}_k, \boldsymbol{\Sigma}_k) \quad \text{(B3)}$$

where $N(\cdot)$ denotes the probability density function of the multivariate normal distribution (**Equation B4**):

$$f(\boldsymbol{m}) = \frac{1}{\sqrt{(2\pi)^D |\boldsymbol{\Sigma}_k|}} \exp\left(-\frac{1}{2}(\boldsymbol{m} - \boldsymbol{\mu}_k)^T \boldsymbol{\Sigma}_k^{-1}(\boldsymbol{m} - \boldsymbol{\mu}_k)\right) \quad \text{(B4)}$$

with $|\Sigma_k|$ representing the determinant of the class-specific covariance matrix. The notation $m^{v(0)} \sim N(\mu_k, \Sigma_k)$ essentially means that random sampling is performed following the probability rule described by $f(m)$. Parameter combinations with higher probability density—corresponding to the most concentrated regions of real core data—are more likely to be selected, whereas those in low-density regions are sampled with lower probability. This sampling strategy ensures that the generated virtual samples are statistically consistent with the distribution of real core samples from the same pore structure class while faithfully preserving the inherent statistical characteristics of the rock-physics rules. Each sampled output yields a complete attribute vector.

The VSG procedure is implemented iteratively to generate virtual samples for each class until the pore structure label in the training set reaches a relatively balanced distribution. In this study, we use the criterion of IR approaching 1 with SR < 0.5 to effectively mitigate class imbalance without excessively diluting authentic core samples.

Appendix C: Pseudo-code for virtual sample generation and hybrid set construction

This appendix presents the complete pseudo-code for the VSG workflow and hybrid training set construction described in **Section 2.2.2**, integrating the class-conditional multivariate Gaussian sampling mechanism detailed in Appendix B.

Require: Real core sample set S^c (each sample with physical property vector $\boldsymbol{m} = [\varphi, \boldsymbol{f}, \boldsymbol{v}, \boldsymbol{\alpha}]$ and pore-structure label y); fast DEM forward model $g(\cdot)$; target imbalance ratio $IR^* \approx 1$ and sample size ratio $SR^* < 0.5$

Fit class-conditional distributions

For each pore-structure class $k \in \{1, 2, 3\}$:

  Extract all real core samples of class k from S^c

  Estimate the Gaussian distribution from real samples

Virtual sample generation

Initialize virtual sample set $S^v = \emptyset$

while $IR(S^c \cup S^v) > IR^*$ **or** $SR(S^c \cup S^v) > SR^*$ **do**

  Select the under-represented class k

  Sample physical property vector $\boldsymbol{m}^{v(0)} \sim \mathcal{N}(\boldsymbol{\mu}_k, \boldsymbol{\Sigma}_k)$

  Assign label $y^{v(0)} = \arg\max\left(\boldsymbol{v}^{v(0)}\right)$

  Compute elastic respons: $\boldsymbol{x}^{v(0)} = g\left(\boldsymbol{m}^{v(0)}\right)$

  Append labeled virtual sample $\left(\boldsymbol{x}^{v(0)}, y^{v(0)}\right)$ into S^v

end while

Hybrid training set construction

Construct hybrid training set $S = S^c \cup S^v$

return S

Figure A1. The pseudo-code for the workflow of hybrid training set construction